



Characterization of the Flagellar Collar Reveals Structural Plasticity Essential for Spirochete Motility

Yunjie Chang,^{a,b} Hui Xu,^c Md A. Motaleb,^c  Jun Liu^{a,b}

^aDepartment of Microbial Pathogenesis, Yale University School of Medicine, New Haven, Connecticut, USA

^bMicrobial Sciences Institute, Yale University, West Haven, Connecticut, USA

^cDepartment of Microbiology and Immunology, Brody School of Medicine, East Carolina University, Greenville, North Carolina, USA

Yunjie Chang and Hui Xu contributed equally to this work.

ABSTRACT Spirochetes are a remarkable group of bacteria with distinct morphology and periplasmic flagella that enable motility in viscous environments, such as host connective tissues. The collar, a spirochete-specific complex of the periplasmic flagellum, is required for this unique spirochete motility, yet it has not been clear how the collar assembles and enables spirochetes to transit between complex host environments. Here, we characterize the collar complex in the Lyme disease spirochete *Borrelia burgdorferi*. We discover as well as delineate the distinct functions of two novel collar proteins, FlcB and FlcC, by combining subtractive bioinformatic, genetic, and cryo-electron tomography approaches. Our high-resolution *in situ* structures reveal that the multiprotein collar has a remarkable structural plasticity essential not only for assembly of flagellar motors in the highly curved membrane of spirochetes but also for generation of the high torque necessary for spirochete motility.

IMPORTANCE Many spirochetes cause serious human diseases. They are well recognized by their distinct morphology and motility. Spirochete motility is driven by a periplasmic flagellum, which possesses a unique collar essential for flagellar assembly and spirochete motility. Here, we discover two novel collar proteins in the Lyme disease spirochete *Borrelia burgdorferi*. We demonstrate, for the first time, that the collar is a multiprotein complex with a remarkable plasticity that enables the motor to accommodate the highly curved membrane of spirochetes and generate the high torque necessary for spirochete motility.

KEYWORDS molecular machine, motility, periplasmic flagella, plasticity, spirochete

Spirochetes are a group of bacteria that cause several serious human diseases, such as Lyme disease (*Borrelia burgdorferi*), syphilis (*Treponema pallidum*), periodontal disease (*Treponema denticola*), and leptospirosis (*Leptospira interrogans*). Spirochetes have a distinctive spiral or flat-wave morphology (1, 2). Enclosing the cell is a multilayered envelope including the outer membrane, peptidoglycan layer, and cytoplasmic membrane. The motility of spirochetes is unique among bacteria, as the whole cell body rotates without any external apparatus. Furthermore, this motility is crucial for host tissue penetration, virulence, and transmission of spirochetes (3–7). The periplasmic flagellum, which rotates between the outer membrane and peptidoglycan layer, is responsible for spirochete motility (1, 2). Each periplasmic flagellum is attached subterminally to one end of the cell poles and extends toward the other end. Spirochete species vary significantly in the number of periplasmic flagella and whether the flagella overlap in the center of the cell (8–12).

Like the external flagella of the model organisms *Escherichia coli* and *Salmonella enterica*, the periplasmic flagellum in spirochetes consists of a motor, hook, and

Editor Lotte Sogaard-Andersen, Max Planck Institute for Terrestrial Microbiology

Copyright © 2021 Chang et al. This is an open-access article distributed under the terms of the [Creative Commons Attribution 4.0 International license](https://creativecommons.org/licenses/by/4.0/).

Address correspondence to Md A. Motaleb, motaleb@ecu.edu, or Jun Liu, jliu@yale.edu.

Received 19 August 2021

Accepted 11 October 2021

Published 23 November 2021

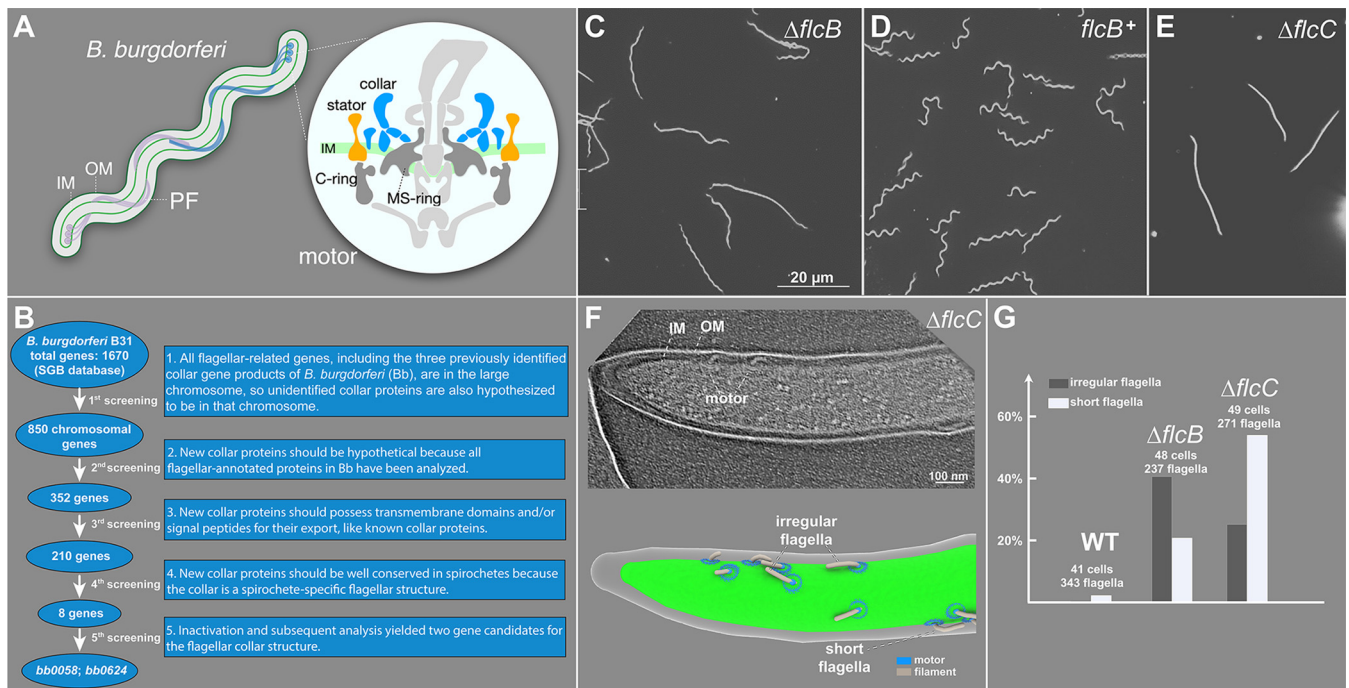


FIG 1 BB0058 (*FlcB*) and BB0624 (*FlcC*) are potential collar proteins in *B. burgdorferi*. (A) Schematic models of the periplasmic flagellum (PF) and motor in a *B. burgdorferi* cell. IM, inner membrane; OM, outer membrane. (B) Based on the common features of the previously identified flagellar collar proteins, all 1,670 gene-encoded proteins of *B. burgdorferi* were manually screened from the Spirochetes Genome Browser (http://sgb.leibniz-flr.de/cgi/list.pl?sid=24&c_sid=yes&ssi=free). Transmembrane domains and signal peptides were predicted using TMHMM, Phobius, and SignalP 5.0 programs. Subsequent screenings resulted in identification of eight potential candidate collar proteins. (C to E) Dark-field microscopic images showing the characteristic rod-shaped morphology of $\Delta flcB$ mutant cells, flat-wave morphology of complemented *flcB*⁺ cells, and rod-shaped morphology of $\Delta flcC$ mutant cells, respectively. (F) A representative tomographic slice of the $\Delta flcC$ cell tip (top) and corresponding 3D surface view (bottom), showing the irregular and short flagella in the mutant cell. (G) Statistical analysis of the flagellar phenotype in WT, $\Delta flcB$, and $\Delta flcC$ cells. A normal flagellum is defined as being oriented toward the other pole of the cell body. An abnormal or irregular periplasmic flagellum is defined as being tilted toward the cell pole from where it originated. The total number of cells and periplasmic flagella analyzed for each strain is shown at the top of the corresponding column.

filament (2, 13). The motor is a rotary machine responsible for the assembly and function of the periplasmic flagellum. Most components of the spirochetal flagellar motor have highly conserved counterparts in the external flagellar motor: the MS ring, C ring, rod, export apparatus, and stator (14–16). Uniquely, a spirochete-specific flagellar component—termed collar—not only contributes to the distinct spirochetal motor structures but also plays a role in recruiting 16 torque-generating stator units (9, 10, 12, 17–22), presumably enabling the increased torque required for spirochetes to swim through complex, viscous host environments (23). The collar structure also contributes to make the spirochetal flagellar motor considerably larger and more complicated than its counterparts in *E. coli* and *S. enterica* (15). However, how the collar supports the production of high torque by the spirochetal flagellar motor has remained poorly understood.

B. burgdorferi has emerged as an ideal model system for understanding the unique structure and function of periplasmic flagella (2, 24). At each cell pole, 7 to 11 periplasmic flagella wrap inward as a flat ribbon along the cell body and overlap in the middle of the cell (Fig. 1A) (11, 25). A combination of genetic and cryo-electron tomography (cryo-ET) approaches has enabled *in situ* visualization of *B. burgdorferi* flagellar motors at an unprecedented resolution, unveiling unique features of this complex machine (16, 24). Specifically, comparative analyses of the wild type, stator deletion mutant $\Delta motB$, and collar deletion mutant $\Delta flbB$ provided direct evidence that the collar is important for stator assembly, flagellar orientation, cell morphology, and motility in *B. burgdorferi* (13, 21, 22). The collar is a large complex consisting of the inner core and the outer, turbine-like structure. Three collar proteins have been identified in *B. burgdorferi* (20–22): *FlbB* (BB0286) appears to serve as the base of the collar structure (21), BB0236 is

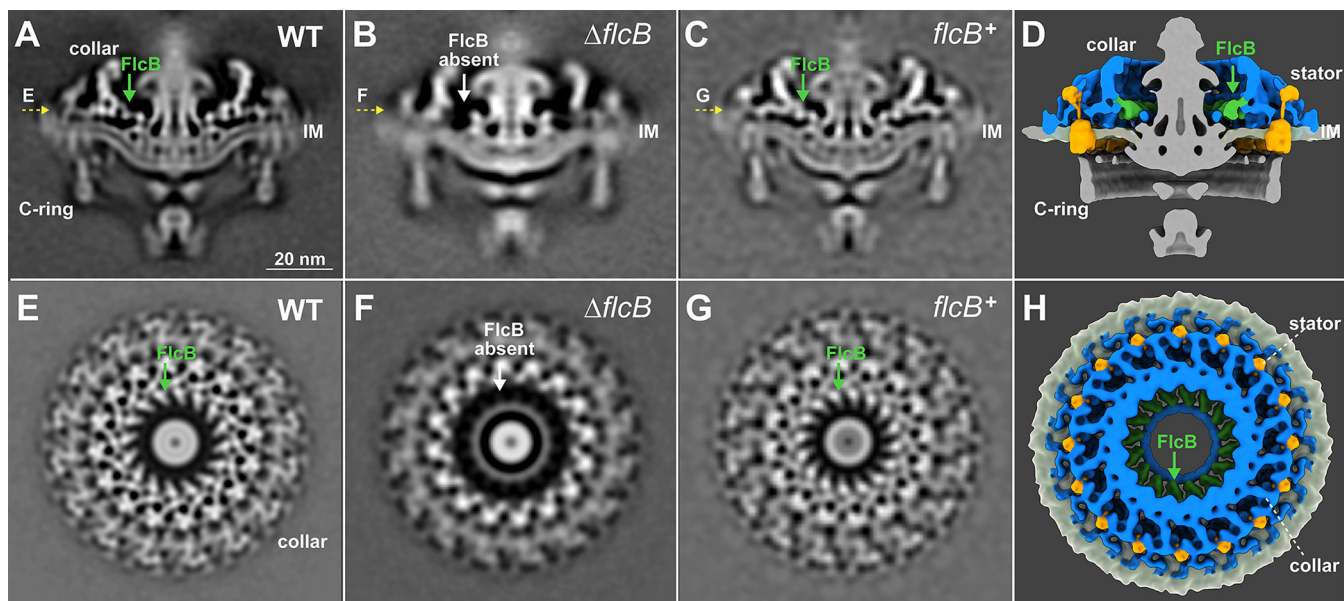


FIG 2 $\Delta flcB$ ($\Delta bb0058$) mutant cells show defects in the flagellar collar structure. (A to C) A central section of the subtomogram averages (16-fold symmetrized) of the WT, $\Delta flcB$, and $flcB^+$ flagellar motors, respectively. The middle portion of the collar is absent in the $\Delta flcB$ motor. (E to G) A top view corresponding to the motor structures shown in panels A to C (indicated by yellow arrows), respectively. (D and H) A cross and top view of the 3D rendering of the WT flagellar motor, respectively. The FlcB protein is shown in green. Only the collar, stator, and inner membrane (IM) are shown in panel H.

involved in collar assembly (22), and FlcA (BB0326) forms the turbine-like structure, directly interacting with the stator units (20). Given that the overall structure of the collar is 79 nm in diameter and ~ 20 nm in height, additional proteins are likely involved in collar assembly. Moreover, the large collar structure must be flexible to accommodate the highly curved membrane at the cell tip (13). How the collar assembles and contributes to stator assembly is essential for understanding the unique spirochete motility.

In this study, we identify two novel collar proteins, FlcB (BB0058) and FlcC (BB0624), each responsible for distinct portions of the collar. Together with studies of other collar proteins (20–22), our high-resolution *in situ* structural analyses of the *B. burgdorferi* flagellar motor provide a molecular basis for the assembly and flexibility of the periplasmic collar complex and its critical roles in the assembly of the stator complexes. Our results also highlight how the collar contributes to the distinct motility that allows spirochetes to swim through complex environments, such as inside ticks and vertebrate hosts.

RESULTS

BB0058 and BB0624 are potential collar proteins. To better understand collar assembly and function, we devised a subtractive bioinformatic approach to identify eight potential collar proteins (Fig. 1B). Each corresponding mutant was constructed and analyzed with respect to motility and morphology phenotypes (see Fig. S1 and S2 in the supplemental material). Two of these genes (*bb0058* and *bb0624*) were ultimately identified as the genes encoding potential collar proteins for the following reasons. (i) $\Delta bb0058$ and $\Delta bb0624$ mutant cells exhibited rod-shaped morphology instead of the characteristic flat-wave morphology in wild-type (WT) spirochetes (Fig. 1C and E). $\Delta bb0058$ mutant cells were significantly less motile than WT cells, whereas the $\Delta bb0624$ mutant cells were completely nonmotile (Fig. S3). These mutants exhibited no polar effects on downstream gene expression. A complemented $\Delta bb0058$ mutant in *cis* ($bb0058^+$) was constructed as described previously (26), and it restored the morphology and motility phenotypes to WT levels (Fig. 1C and D and Fig. S3). (ii) Domain analysis data suggest that BB0058 possesses multiple tetratricopeptide repeat (TPR) domains, and both BB0058 and BB0624 possess a signal peptide at their N-terminal region that is likely required for their

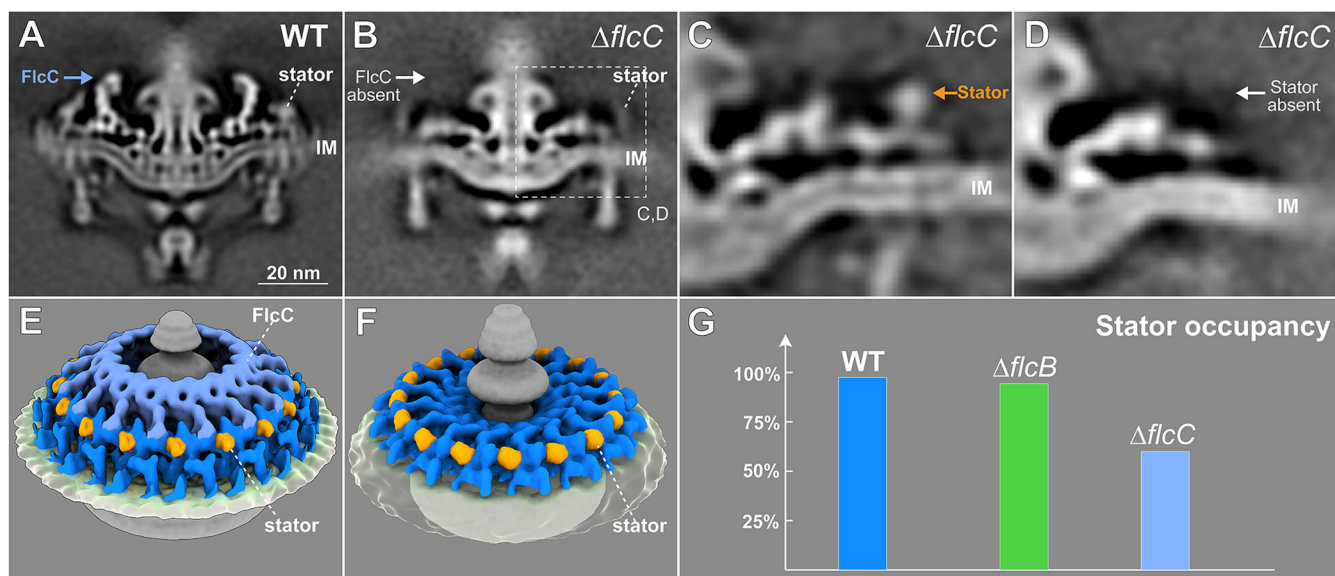


FIG 3 $\Delta flcC$ mutant cells show defects in the collar structure and have fewer stator units assembled in the motor. (A and B) A central section of the subtomogram average (16-fold symmetrized) of WT and $\Delta flcC$ flagellar motors, respectively. The top portion of the collar (indicated by a white arrow) is absent from the $\Delta flcC$ motor. (C and D) Class averages of the collar region (dashed box in panel B) with and without the density of the stator complex in the $\Delta flcC$ motor, respectively. (E and F) A tilted side view of the 3D rendering of WT and $\Delta flcC$ flagellar motors (with stator complexes), respectively. (G) A histogram showing stator occupancy in the WT, $\Delta flcB$, and $\Delta flcC$ motors, respectively. Refer to Materials and Methods section for details about the calculation of stator occupancy.

export across the membrane (not shown in current work). (iii) Cryo-ET reconstructions of the cell tips indicate that the $\Delta bb0058$ and $\Delta bb0624$ cells possess approximately 40% and 34% fewer flagella than WT cells (Fig. 1G), respectively. In addition, the flagella in both $\Delta bb0058$ and $\Delta bb0624$ cells appear to show shorter lengths and abnormal orientations (Fig. 1F and G), with filaments extending toward their pole of origin instead of toward the other cell pole, as in WT cells. Similar shorter length and abnormal orientation phenotypes were also observed in our previously reported collar gene mutants (20).

FlcB is a novel flagellar protein that contributes to the middle portion of the collar. To determine whether BB0058 is involved in assembly of the collar complex, we used cryo-ET and subtomogram averaging to resolve the *in situ* structures of the flagellar motor in $\Delta bb0058$ and $bb0058^+$ cells. Compared to the WT motor (Fig. 2A and E), a bridge-like structure near the interface between the collar and the MS ring is absent from the $\Delta bb0058$ motor (Fig. 2B and F), but this structure is restored in the complemented $bb0058^+$ motor (Fig. 2C and G), suggesting that BB0058 is responsible for the formation of the bridge-like structure of the collar (Fig. 2D and H). We therefore renamed BB0058 periplasmic flagellar collar protein B (FlcB). Notably, in the spirochetal flagellar motor, 16 copies of this bridge-like structure form the FlcB ring directly above the MS ring (Fig. 2D and H). The FlcB ring does not directly interact with the stator complexes or the MS ring yet has a significant impact on flagellar rotation and bacterial motility.

FlcC is a novel flagellar protein responsible for collar and stator assembly. To identify specific roles of the BB0624 protein, we determined the *in situ* structure of the $\Delta bb0624$ motor by cryo-ET and subtomogram averaging, revealing that the top portion of the collar is absent (Fig. 3B). BB0624 is therefore a collar protein, renamed hereafter periplasmic flagellar collar protein C (FlcC). Furthermore, the densities corresponding to the stator complexes in the $\Delta flcC$ motor are considerably different from those in the WT motor, suggesting that FlcC directly impacts not only collar formation but also stator assembly. To estimate stator complex numbers in WT and these two new mutants, focused alignment and classification were utilized to analyze the stator densities. For the $\Delta flcC$ mutant, the class with stator density (Fig. 3C) accounts for ~40% of the total collar subunits, while the class without stator density (Fig. 3D) accounts for ~60%, indicating

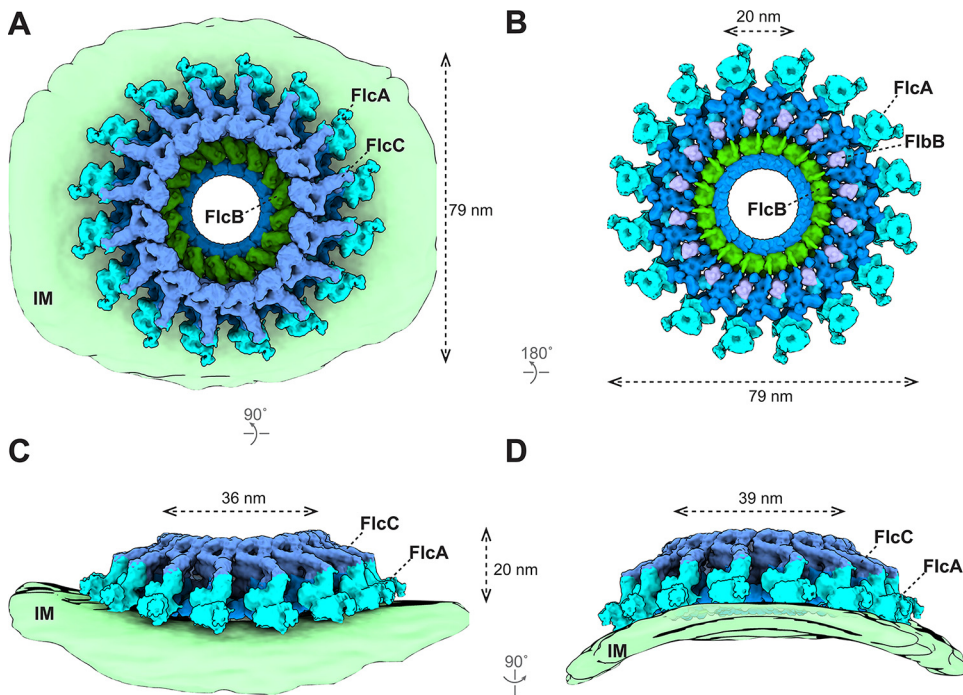


FIG 4 Structure of the flagellar collar in $\Delta motB$ *B. burgdorferi*. (A to D) 3D surface view of the whole collar complex in $\Delta motB$ *B. burgdorferi*. The collar is ~ 79 nm in diameter and embeds on the IM. Each known collar protein has 16 copies and assembles into a ring structure. The membrane of the spirochetal cells shows a clear curvature and distorts the collar complex (C and D). The height of the collar is 20 nm on the flat IM (C) and 23 nm on the curved IM (D). The inner diameter of the FlcC ring is 36 nm on the flat IM (C) and 39 nm on the curved IM (D). The FlcA proteins are colored in ice, FlcB in green, FlcC in light blue, and FlbB in purple. The unknown collar proteins are colored in dark blue.

that stator occupancy in the $\Delta flcC$ motor is $\sim 40\%$, considerably lower than in the WT ($\sim 96\%$) and $\Delta flcB$ motors ($\sim 94\%$). This result is consistent with immunoblotting data showing that the stator protein MotB is significantly reduced in the $\Delta flcC$ mutant compared to WT cells (Fig. S2C). Collectively, these results support the model that FlcC functions as a major collar protein directly involved in collar formation and stator assembly.

The molecular architecture of the collar reveals its intrinsic plasticity. Five collar proteins have been identified and characterized in *B. burgdorferi*: FlbB (21), BB0236 (22), FlcA (20), FlcB (BB0058), and FlcC (BB0624). To understand how these proteins assemble as the complex collar, we developed a sophisticated approach to analyze the collar structure in the absence of the stator complexes. First, we generated an asymmetric reconstruction of the $\Delta motB$ motors (Fig. S4A and B) (13). The asymmetric reconstruction reveals 16 collar subunits and their associated membrane curvature (Fig. S4C), consistent with the observation that the motors are embedded in a highly curved membrane cylinder. Second, to determine the collar subunit structure at higher resolution, we extracted 16 collar subunits from each motor and performed three-dimensional (3D) classification and focused refinement (see Fig. S4D and S4E and Movie S1 in the supplemental material). Third, the high-resolution structure of the collar subunit was then mapped back to the asymmetric reconstruction of the $\Delta motB$ motor structure to obtain a detailed overview of the collar complex (Fig. 4). The exact location of each collar protein was defined by comparing the high-resolution *in situ* structure of the $\Delta motB$ motor with specific collar mutant structures reported in this study (Fig. 2 and 3) and previously (20–22) and analyzing the protein-protein interaction data (Fig. S5). In the large collar complex (79 nm in diameter) (Fig. 4A and B), FlcA is closely associated with the membrane and forms the turbine-like structure (Fig. 4). FlbB forms the base of the collar (Fig. 4B). FlcC is located on top of the collar structure

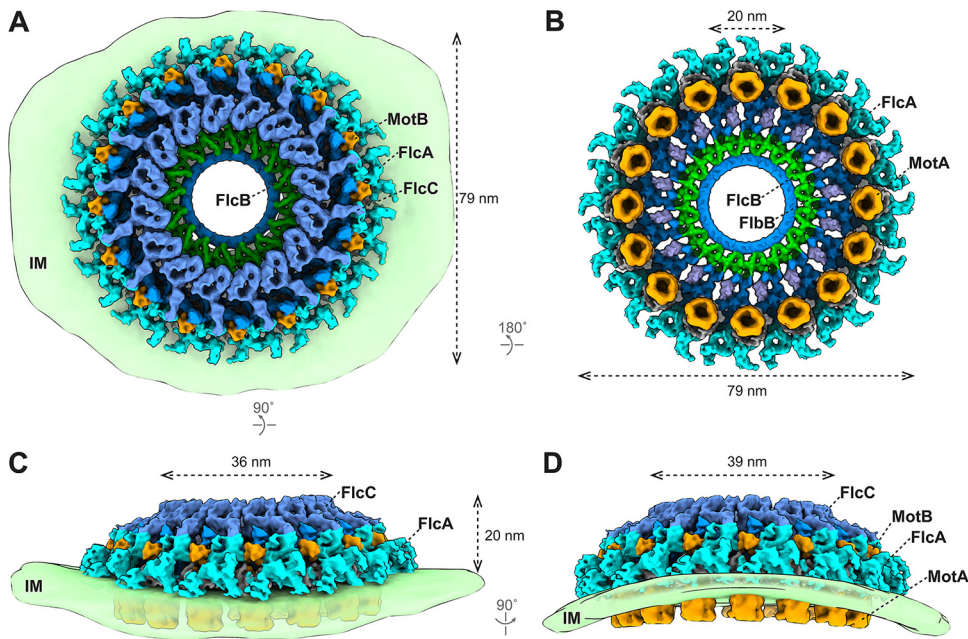


FIG 5 The collar facilitates the assembly of 16 stator complexes in a highly curved membrane. (A to D) 3D surface view of the whole collar complex in WT *B. burgdorferi*. The diameter and height of the collar are indicated. The curvature of the IM is clearly resolved in the asymmetric reconstruction of the motor structure (C and D). Sixteen stator units embed on the IM and are surrounded by the collar proteins. FlcA directly interacts with the stator units. The color scheme is the same as in Fig. 4.

(Fig. 4A, C, and D), and FliB is located approximately in the middle of the collar complex (Fig. 4B). Although some components of the collar remain undefined, it is evident that the collar complex is composed of multiple different proteins, each contributing to a distinct portion of the highly modular, flexible architecture of the collar complex. Importantly, this highly modular architecture of the collar enables extensive remodeling to accommodate the curvature of the membrane cylinder, which is ubiquitous in spirochetes and other bacteria (Fig. 4C and D).

The collar facilitates the assembly and function of the stator complexes. The collar is important for stator assembly and recruitment in spirochetes (21). To determine the detailed interactions between the collar and stator complexes, we analyzed WT motors (Fig. S4G to K) and determined the high-resolution asymmetric reconstruction of the collar (Fig. 5). The overall size and shape of the collar remain similar in both WT and Δ *motB* motors (Fig. 4 and 5). In the WT motor, 16 stator units are closely associated with the collar complex through multiple interactions. The periplasmic domain of the stator complex directly interacts with FliA and additional unknown collar proteins (Fig. 5 and Fig. S4J), likely stabilizing its assembly around the motor. Furthermore, 16 stator complexes appear perfectly embedded in the curved membrane cylinder around the motor. By contrast, the stator complexes fail to assemble around the motor in the absence of the entire collar or its periphery (20–22). Therefore, the collar has evolved a remarkable modular architecture ideal not only to recruit the stator complexes but also to stabilize the stator ring with 16 complexes around the motor, thus ensuring maximal torque generation (Fig. 5).

DISCUSSION

Spirochete motility is unique among bacteria, due to the location and distinct assembly of periplasmic flagella. It is increasingly evident that the periplasmic flagellum possesses a specialized multiprotein collar important for the assembly of periplasmic flagella and motility of spirochetes. Five spirochete-specific collar proteins in *B.*

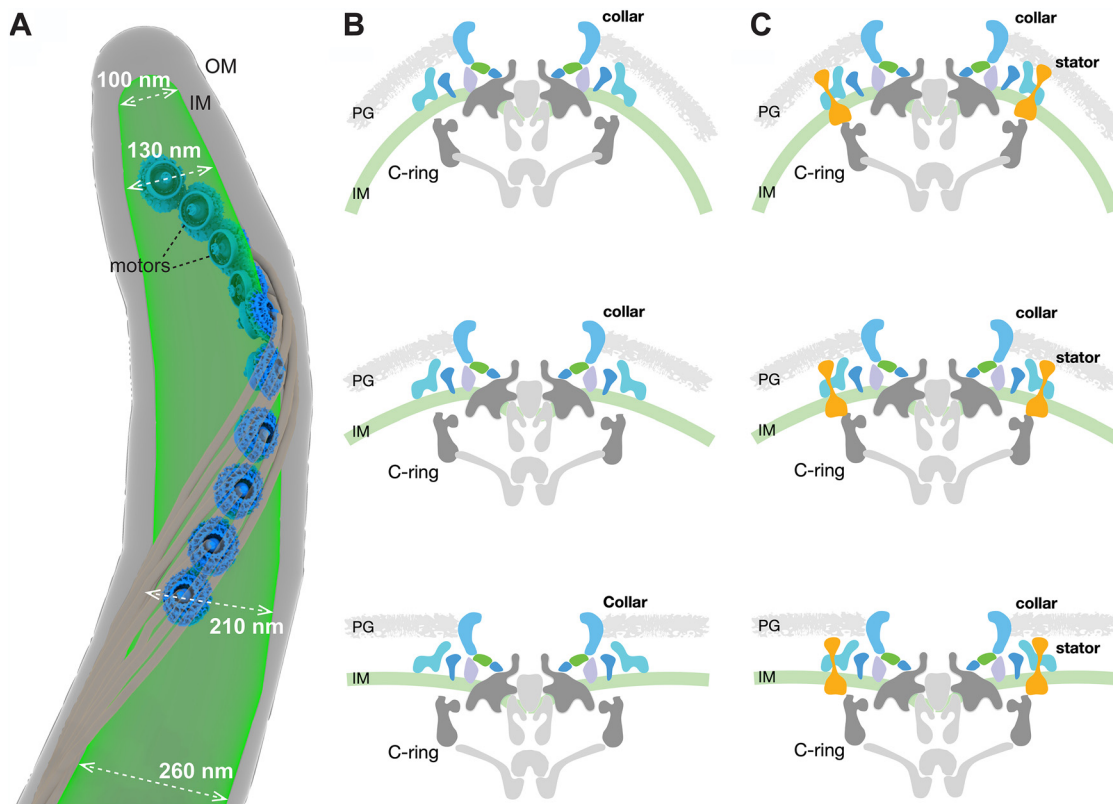


FIG 6 The mosaic collar complex changes conformation to accommodate the inner membrane curvature in *B. burgdorferi*. (A) Surface rendering of a representative WT cell tip. Ten motors embed in the IM and distribute along the cell tip. The diameter of the IM at different positions at the cell tip is indicated. Note that the IM is more curved (has a smaller diameter) at the positions closer to the cell tip. (B and C) The flagellar motor embeds on the IM and is distorted due to the IM curvature. The periplasmic collar complex surrounds the stator units and can change conformation to fit the IM curvature, facilitating the assembly and function of spirochetal motors in highly curved membrane environments. PG, peptidoglycan.

burgdorferi have been demonstrated to be involved in collar assembly. Given that these collar proteins are well conserved in spirochetes, their homologs are likely involved in collar assembly across diverse spirochetes (14, 15).

The $\Delta flcB$ and $\Delta flcC$ mutants produced shorter and irregular periplasmic flagella (Fig. 1G). We have also observed shorter and/or irregular flagella in our previously published $\Delta flbB$, $\Delta bb0236$, and $\Delta flcA$ collar mutants and in the $\Delta flil$ mutant (20–22, 27). Furthermore, some of the $\Delta motB$ mutant's periplasmic flagella are shorter than those of wild-type cells (4). While we do not fully understand why these mutants are more likely to have shorter flagella, we speculate that the assembly of periplasmic flagella is a highly coordinated process; therefore, any defects in the motor proteins may have a profound impact on overall morphology and motility.

One of the most remarkable features of *B. burgdorferi* is that multiple flagellar motors are embedded in the inner membrane cylinder in a highly organized pattern (Fig. 6A). As a result, the cell cylinder diameter varies remarkably, ranging from ~100 nm to ~300 nm (Fig. 6A). The collar must therefore be highly flexible to accommodate variable membrane curvatures (Fig. 6B and C; see also Movie S2 in the supplemental material). Indeed, our studies have clearly demonstrated that the collar has a highly modular architecture due to the highly coordinated assembly of multiple spirochete-specific proteins (including several transmembrane proteins). This modular architecture may be of key importance for facilitating the remarkable plasticity of the collar. Moreover, multiple collar proteins directly interact with the stator complexes. Therefore, the unique plasticity of the collar also facilitates the recruitment and stabilization of maximal numbers of stator

complexes around the motor even in highly curved membrane environments (Fig. 6B and C and Movie S2). That the entire flagellar motor remodels and adapts to accommodate variable membrane environments is crucial to generate the highest torques required to constantly drive the motility of spirochetes and benefit their distinct lifestyle.

In summary, we have identified and characterized multiple novel collar proteins in *B. burgdorferi*, providing a molecular basis for understanding the remarkable structural plasticity of this multiprotein spirochetal complex. The collar not only enables the assembly of the motor in the curved membrane of spirochetes but also provides a structural scaffold for stator recruitment and stabilization, both essential for the function of periplasmic flagella and motility in spirochetes. Identification of additional collar proteins based on the protein-protein interactions, along with high-resolution *in situ* structural analyses, will provide further insights into how the structural plasticity of the collar is required for motility in spirochetes.

MATERIALS AND METHODS

Bacterial strains and growth conditions. High-passage *B. burgdorferi* strain B31-A was used as the wild-type (WT) clone throughout this study (28, 29). The $\Delta bb0058$ ($\Delta flcB$) and $\Delta bb0624$ ($\Delta flcC$) mutants and complemented *flcB*⁺ strains were constructed as described below. *B. burgdorferi* cells were cultivated in liquid Barbour-Stoenner-Kelly (BSK-II) broth or agarose plates and incubated at 35°C in a 2.5% CO₂ incubator, as reported previously (30, 31). Antibiotics, when required, were included in the *B. burgdorferi* medium at the following concentrations: 200 μ g/ml kanamycin and/or 100 μ g/ml streptomycin. *Escherichia coli* strains were grown at room temperature or 37°C in liquid Luria-Bertani (LB) broth or plated on LB agar (32, 33). When required, 100 μ g/ml ampicillin, 100 μ g/ml spectinomycin, 0.2% glucose, 80 μ g/ml 5-bromo-4-chloro-3-indolyl- β -D-galactopyranoside (X-Gal), and/or 0.5 mM isopropyl- β -D-1-thiogalactopyranoside (IPTG) were added to LB medium as supplements.

Bioinformatics. Basic local alignment search tool (BLAST) (34, 35) was utilized to determine protein or gene homologs from the sequence database. The lower the E-value (lower than 0), the more significant the score is. Signal peptides were predicted using SignalP 5.0 and Phobius programs (36–38). Protein domains were analyzed using the Conserved Domain Database (39, 40) and Pfam (41, 42).

Overexpression of recombinant proteins in *E. coli*. To express the *B. burgdorferi* BB0058 (FlcB) protein in *E. coli*, a DNA fragment harboring the BB0058 open reading frame (ORF) without the signal peptide region (1 to 20 amino acids [aa]) was PCR amplified from chromosomal DNA of *B. burgdorferi* B31-A cells using primers PF MBP0058_BamHI (CGTCGACGGATCCGATACTACAGCATTAGGACATTATC) and PR MBP0058_PstI (TTAATTACCTGCAGTTATCTTTTTATAAGCACAGTGGCTC) (restriction sites are underlined) and cloned into the pMAL c5x (NEB Inc.) using BamHI and PstI restriction sites to produce the maltose-binding protein (MBP)-BB0058 protein. MBP-MotB was similarly generated. In brief, the coding sequence of MBP from pMAL c5x was fused to the 3' end of the coding region of MotB without its transmembrane domain, aa 1 to 44 using PCR, and then cloned into pET28a(+) (Novagen Inc.). Similarly, 1 \times FLAG (DYKDDDDK)-tagged BB0624 (FlcC) and FlcA (BB0326) were constructed for affinity blotting. In brief, 1 \times FLAG tag coding sequence (GACTACAAAGACGATGACGACAAG) was fused to the coding regions of BB0624 without the signal peptide region, aa 1 to 22 and the C terminus aa 360 to 931 of BB0326 using PCR amplification with primers PF MBP0624_BamHI (CGTCGACGGATCCGATTACAAGGCCCTTGATTTTAAATC) and PR MBP0624FLAGc_PstI (TAATTACCTGCAGTTACTTGTCTGCATCGTCTTTGTAGTCCTTTTCTTAATGCCAGTATTTTG), PF HisThro BB326C572aa_NdeI (GGCAGCCATATGGCCTCTGAGAGCAAGTATAAAGAG), and PR PR BB0326C572aaFLAGc_NotI (GACGATATCGCGGCCGCTTACTTGTCTGCATCGTCTTTGTAGTCAAGTTTTTCGGATAAATTTTC), respectively, which were then cloned into pMAL c5x (NEB Inc.). Expression of MBP, MBP-MCP5, -Flil, -FliB, -BB0236, -FlcA and FLAG-MotB, -FliB, -BB0236, and -Flil were described elsewhere (20–22).

All *E. coli* strains were induced with 0.5 mM IPTG at room temperature, and purifications of recombinant proteins were performed using amylose resin for MBP-tagged proteins and HisPure Ni-nitriloacetic acid (NTA) resin for His-tagged proteins.

SDS-PAGE, immunoblotting, and affinity blotting. Sodium dodecyl sulfate-polyacrylamide gel electrophoresis (SDS-PAGE) was performed as described previously (31, 43, 44). Exponentially growing *B. burgdorferi* cells were harvested, washed with phosphate-buffered saline (PBS), and resuspended in the same buffer to process the preparation of cell lysate for SDS-PAGE. Immunoblotting with *B. burgdorferi* FlaB-, MotB-, FliB-, Flil-, FliG1-, and DnaK-specific antibodies (6, 21, 27, 45–47) was performed using Pierce enhanced chemiluminescence Western blotting substrate (Thermo Fisher Scientific). Protein concentrations were determined using a Bio-Rad protein assay kit with bovine serum albumin as the standard. Unless specified, approximately 10 μ g of cell lysates were subjected to SDS-PAGE.

Far Western or affinity blot assays were performed as described previously (20–22, 48, 49). In brief, 1 μ g purified recombinant proteins was subjected to SDS-PAGE and transferred to polyvinylidene difluoride membranes. The membranes were blocked in the blocking solution (5% skim milk, 10 mM Tris, 150 mM NaCl, and 0.3% Tween 20 [pH 7.4]) with gentle shaking for 4 to 6 h at room temperature and then incubated with purified 1 \times FLAG-tagged protein at a 2- μ g/ml concentration in blocking solution overnight. The membranes were washed three times with washing buffer (10 mM Tris, 150 mM NaCl, and 0.3% Tween 20 [pH 7.4]) and then probed with monoclonal anti-FLAG M2 antibody (Sigma-Aldrich Co. LLC).

Construction of the *bb0058* and *bb0624* mutants and *bb0058* complemented strain. Construction of the *bb0058* (*flcB*) and *bb0624* (*flcC*) inactivation plasmid, electroporation, and plating of *B. burgdorferi* were performed as described earlier (31, 43, 50, 51). *bb0058* and *bb0624* were inactivated individually using a promoterless kanamycin resistance cassette (*Pl-Kan*), as reported in detail (50). The Δ *bb0058* mutant strain was complemented in *cis* by chromosomal integration using the pXLF14301 suicide vector as described previously (26, 52). In brief, the native promoter regions of the *bb0058* (P_{bb0061}) and *bb0058* genes were separately PCR amplified from WT *B. burgdorferi* strain B31-A genomic DNA using primer pair PF Pbb0061bb0058SpeI (TGTCTAGAACTAGTCCGGCTATTAATGTTTTTCGCAATC) and P1R Pbb0061bb0058 (AAAAACCAATTAATAATTCATATATTTTACATGCCCCCTA) and primer pair P2F Pbb0061bb0058 (TAGGGGGGCATGTAATAATATGAAATTTAATTGTTTTT) and PR Pbb0061bb0058NotI (CTCGGGTAGCGGCCGCTATCTTTTATAAGCACAGTGGC) and fused together by overlapping PCR to generate P_{bb0061} -*bb0058*, which was inserted into derivative pXLF14301: P_{flgB} -*Strep* (53–56) using SpeI and NotI restriction sites, yielding pXLFbb0058. The plasmid was then electroporated into the Δ *bb0058* mutant cells, followed by selection with both kanamycin and streptomycin. The resistant clones were analyzed by PCR to verify the integration of P_{bb0061} -*bb0058*- P_{flgB} -*Strep* within the intergenic region of *bb0445* and *bb0446*. Multiple attempts to complement the Δ *bb0624* mutant in *cis* or in *trans* were unsuccessful, as it is well known that genetic manipulations in *B. burgdorferi* are challenging (21, 57–64).

Dark-field microscopy and swarm plate assays. Exponentially growing *B. burgdorferi* cells were observed using a Zeiss Axio Imager M1 dark-field microscope connected to an AxioCam digital camera to determine bacterial morphology, as described previously (30, 65). Swarm plate motility assay was also performed using our established protocol (30).

Cryo-ET data collection and tomogram reconstruction. Frozen-hydrated specimens were prepared as described previously (17). In brief, various clones of exponentially growing *B. burgdorferi* cells were centrifuged individually at $5,000 \times g$ for ~5 min, and the resulting pellets were suspended in PBS to achieve a cell concentration of $\sim 1 \times 10^8$ /ml. After adding 10-nm gold marker solution, 5 μ l of the cell suspension was placed on freshly glow-discharged (for ~25 s) holey carbon grids (Quantifoil Cu R2/1, 200 mesh). The grids were front blotted with Whatman filter paper and rapidly frozen in liquid ethane, using a homemade plunger apparatus as described previously (17). The grids were then imaged using a 300-kV electron microscope (Titan Krios; Thermo Fisher Scientific) equipped with a field emission gun, a Volta phase plate (VPP), and a post-Gatan imaging filter (GIF) direct electron detector (Gatan K2 Summit or K3 Summit). Serial EM was used to collect all tilt series (66). The defocus was set as close to 0 μ m as possible for those tilt series collected with VPP, while the defocus was set ca. -3μ m for those collected without VPP. A total dose of $\sim 80 \text{ e}^-/\text{\AA}^2$ is distributed among 35 (or 33) tilt images covering angles from -51° to 51° (or from -48° to 48°) with a tilt step of 3° .

All recorded images were first motion corrected using MotionCorr2 (67) and then stacked and aligned by IMOD (68). For the data collected with VPP, the aligned tilt series were directly used to reconstruct tomograms by weighted back-projection using IMOD or by simultaneous iterative reconstruction technique (SIRT) reconstruction using Tomo3D (69). For the data collected without VPP, Gctf (70) was used to determine the defocus of each tilt image in the aligned stacks, and the “ctfphaseflip” function in IMOD was used to do the contrast transfer function (CTF) correction for the tilt images. The tomograms were then reconstructed using IMOD or Tomo3D. The number of tomograms used in this work for each strain is shown in Table S1 in the supplemental material.

Subtomogram analysis. Bacterial flagellar motors were manually picked from the $6 \times$ binned tomograms. The subtomograms of flagellar motors were analyzed by i3 software package (71, 72). Afterwards, the subtomograms were extracted from unbinned tomograms with the refined positions and further binned by 2 or 4 based on the requirement for alignment and classification.

(i) Focused refinement of collar region. Each flagellar motor has 16 collar subunits. After alignment for the whole motor structure, the regions around 16 collar subunits were first extracted from each motor, and then we refined the 3D alignment and applied 3D classification based on the density of the collar subunit to remove particles with bad contrast or large distortions to obtain the refined structures. The number of flagellar motor and collar subunits used for subtomogram averaging is shown in Table S1.

(ii) Measurement of stator occupancy. For the WT, Δ *flcB*, and Δ *flcC* motors, we first performed focused refinement to the collar region as described previously. Then 3D classification was applied to all collar subunits based on the density of the stator complex. The class averages with density of the stator complex were considered as having assembled stator units, while the class averages without density of the stator complex were considered as having no assembled stator units. The number of collar subunits with stator units was divided by the total number of collar subunits to calculate stator occupancy. Fourier shell correlation (FSC) coefficients were calculated by generating the correlation between two randomly divided halves of the aligned images used to estimate the resolution and to generate the final maps.

Three-dimensional visualization. UCSF Chimera (73) and ChimeraX (74) were used for 3D visualization and surface rendering of subtomogram averages of the whole motor or collar subunit. For the 3D surface views of the whole collar complex shown in Fig. 4 and 5, the surface view of each collar protein in the Δ *motB* or WT strain was first segmented by ChimeraX and then fitted to the collar complex of the asymmetric reconstructed motor structure, using the “fitmap” command in ChimeraX. Segmentations of representative reconstructions from WT and Δ *flcC* cell tips were manually constructed using IMOD (68).

SUPPLEMENTAL MATERIAL

Supplemental material is available online only.

MOVIE S1, MOV file, 2.8 MB.

MOVIE S2, MOV file, 15.6 MB.

FIG S1, TIF file, 1.7 MB.

FIG S2, TIF file, 2 MB.

FIG S3, TIF file, 0.2 MB.

FIG S4, TIF file, 2.2 MB.

FIG S5, TIF file, 1.2 MB.

TABLE S1, PDF file, 0.2 MB.

ACKNOWLEDGMENTS

We thank Jennifer Aronson for critical reading of the manuscript. We thank Jun He and Shenping Wu for assisting cryo-ET data collection.

Y.C. and J.L. were supported by grant R01AI087946; H.X. and M.A.M. were supported by R01AI132818 from National Institute of Allergy and Infectious Diseases (NIAID) and National Institutes of Health (NIH). Part of cryo-ET data were collected at Yale CryoEM resource that is funded in part by NIH grant 1S10OD023603-01A1.

REFERENCES

- Nakamura S. 2020. Spirochete flagella and motility. *Biomolecules* 10:550. <https://doi.org/10.3390/biom10040550>.
- Charon NW, Cockburn A, Li C, Liu J, Miller KA, Miller MR, Motaleb MA, Wolgemuth CW. 2012. The unique paradigm of spirochete motility and chemotaxis. *Annu Rev Microbiol* 66:349–370. <https://doi.org/10.1146/annurev-micro-092611-150145>.
- Motaleb MA, Liu J, Wooten RM. 2015. Spirochetal motility and chemotaxis in the natural enzootic cycle and development of Lyme disease. *Curr Opin Microbiol* 28:106–113. <https://doi.org/10.1016/j.mib.2015.09.006>.
- Sultan SZ, Sekar P, Zhao X, Manne A, Liu J, Wooten RM, Motaleb MA. 2015. Motor rotation is essential for the formation of the periplasmic flagellar ribbon, cellular morphology, and *Borrelia burgdorferi* persistence within *Ixodes scapularis* tick and murine hosts. *Infect Immun* 83:1765–1777. <https://doi.org/10.1128/IAI.03097-14>.
- Lambert A, Picardeau M, Haake DA, Sermswan RW, Srikrum A, Adler B, Murray GA. 2012. FlaA proteins in *Leptospira interrogans* are essential for motility and virulence but are not required for formation of the flagellum sheath. *Infect Immun* 80:2019–2025. <https://doi.org/10.1128/IAI.00131-12>.
- Li C, Xu H, Zhang K, Liang FT. 2010. Inactivation of a putative flagellar motor switch protein Flg1 prevents *Borrelia burgdorferi* from swimming in highly viscous media and blocks its infectivity. *Mol Microbiol* 75:1563–1576. <https://doi.org/10.1111/j.1365-2958.2010.07078.x>.
- Lux R, Miller JN, Park NH, Shi W. 2001. Motility and chemotaxis in tissue penetration of oral epithelial cell layers by *Treponema denticola*. *Infect Immun* 69:6276–6283. <https://doi.org/10.1128/IAI.69.10.6276-6283.2001>.
- Wunder EA, Figueira CP, Benaroudj N, Hu B, Tong BA, Trajtenberg F, Liu J, Reis MG, Charon NW, Buschiazio A, Picardeau M, Ko AI, Jr. 2016. A novel flagellar sheath protein, FcpA, determines filament coiling, translational motility and virulence for the *Leptospira* spirochete. *Mol Microbiol* 101:457–470. <https://doi.org/10.1111/mmi.13403>.
- Izard J, Renken C, Hsieh C-E, Desrosiers DC, Dunham-Ems S, La Vake C, Gebhardt LL, Limberger RJ, Cox DL, Marko M, Radolf JD. 2009. Cryo-electron tomography elucidates the molecular architecture of *Treponema pallidum*, the syphilis spirochete. *J Bacteriol* 191:7566–7580. <https://doi.org/10.1128/JB.01031-09>.
- Raddi G, Morado DR, Yan J, Haake DA, Yang XF, Liu J. 2012. Three-dimensional structures of pathogenic and saprophytic *Leptospira* species revealed by cryo-electron tomography. *J Bacteriol* 194:1299–1306. <https://doi.org/10.1128/JB.06474-11>.
- Zhang K, He J, Cantalano C, Guo Y, Liu J, Li C. 2020. FlhF regulates the number and configuration of periplasmic flagella in *Borrelia burgdorferi*. *Mol Microbiol* 113:1122–1139. <https://doi.org/10.1111/mmi.14482>.
- Liu J, Howell JK, Bradley SD, Zheng Y, Zhou ZH, Norris SJ. 2010. Cellular architecture of *Treponema pallidum*: novel flagellum, periplasmic cone, and cell envelope as revealed by cryo electron tomography. *J Mol Biol* 403:546–561. <https://doi.org/10.1016/j.jmb.2010.09.020>.
- Chang Y, Moon KH, Zhao X, Norris SJ, Motaleb MA, Liu J. 2019. Structural insights into flagellar stator-rotor interactions. *Elife* 8:e48979. <https://doi.org/10.7554/eLife.48979>.
- Chen S, Beeby M, Murphy GE, Leadbetter JR, Hendrixson DR, Briegel A, Li Z, Shi J, Tocheva EI, Müller A, Dobro MJ, Jensen GJ. 2011. Structural diversity of bacterial flagellar motors. *EMBO J* 30:2972–2981. <https://doi.org/10.1038/emboj.2011.186>.
- Zhao X, Norris SJ, Liu J. 2014. Molecular architecture of the bacterial flagellar motor in cells. *Biochemistry* 53:4323–4333. <https://doi.org/10.1021/bi5000059y>.
- Carroll BL, Liu J. 2020. Structural conservation and adaptation of the bacterial flagella motor. *Biomolecules* 10:1492. <https://doi.org/10.3390/biom10111492>.
- Liu J, Lin T, Botkin DJ, McCrum E, Winkler H, Norris SJ. 2009. Intact flagellar motor of *Borrelia burgdorferi* revealed by cryo-electron tomography: evidence for stator ring curvature and rotor/C-ring assembly flexion. *J Bacteriol* 191:5026–5036. <https://doi.org/10.1128/JB.00340-09>.
- Murphy GE, Leadbetter JR, Jensen GJ. 2006. In situ structure of the complete *Treponema primitia* flagellar motor. *Nature* 442:1062–1064. <https://doi.org/10.1038/nature05015>.
- Kudryashev M, Cyrklaff M, Baumeister W, Simon MM, Wallich R, Frischknecht F. 2009. Comparative cryo-electron tomography of pathogenic Lyme disease spirochetes. *Mol Microbiol* 71:1415–1434. <https://doi.org/10.1111/j.1365-2958.2009.06613.x>.
- Xu H, He J, Liu J, Motaleb MA. 2020. BB0326 is responsible for the formation of periplasmic flagellar collar and assembly of the stator complex in *Borrelia burgdorferi*. *Mol Microbiol* 113:418–429. <https://doi.org/10.1111/mmi.14428>.
- Moon KH, Zhao X, Manne A, Wang J, Yu Z, Liu J, Motaleb MA. 2016. Spirochetes flagellar collar protein FlbB has astounding effects in orientation of periplasmic flagella, bacterial shape, motility, and assembly of motors in *Borrelia burgdorferi*. *Mol Microbiol* 102:336–348. <https://doi.org/10.1111/mmi.13463>.
- Moon KH, Zhao X, Xu H, Liu J, Motaleb MA. 2018. A tetratricopeptide repeat domain protein has profound effects on assembly of periplasmic flagella, morphology and motility of the Lyme disease spirochete *Borrelia burgdorferi*. *Mol Microbiol* 110:634–647. <https://doi.org/10.1111/mmi.14121>.
- Beeby M, Ribardo DA, Brennan CA, Ruby EG, Jensen GJ, Hendrixson DR. 2016. Diverse high-torque bacterial flagellar motors assemble wider stator rings using a conserved protein scaffold. *Proc Natl Acad Sci U S A* 113:E1917–E1926. <https://doi.org/10.1073/pnas.1518952113>.
- Chang Y, Liu J. 2019. Architecture and assembly of periplasmic flagellum. *Microbiol Spectr* 7:10.1128/microbiolspec.PSIB-0030-2019. <https://doi.org/10.1128/microbiolspec.PSIB-0030-2019>.
- Charon NW, Goldstein SF, Marko M, Hsieh C, Gebhardt LL, Motaleb MA, Wolgemuth CW, Limberger RJ, Rowe N. 2009. The flat-ribbon configuration of the periplasmic flagella of *Borrelia burgdorferi* and its relationship to motility and morphology. *J Bacteriol* 191:600–607. <https://doi.org/10.1128/JB.01288-08>.
- Pitzer JE, Sultan SZ, Hayakawa Y, Hobbs G, Miller MR, Motaleb MA. 2011. Analysis of the *Borrelia burgdorferi* cyclic-di-GMP-binding protein PlzA reveals a role in motility and virulence. *Infect Immun* 79:1815–1825. <https://doi.org/10.1128/IAI.00075-11>.

27. Motaleb MA, Pitzer JE, Sultan SZ, Liu J. 2011. A novel gene inactivation system reveals altered periplasmic flagellar orientation in a *Borrelia burgdorferi* flil mutant. *J Bacteriol* 193:3324–3331. <https://doi.org/10.1128/JB.00202-11>.
28. Bono JL, Elias AF, Kupko JJ, Stevenson B, Tilly K, Rosa P. 2000. Efficient targeted mutagenesis in *Borrelia burgdorferi*. *J Bacteriol* 182:2445–2452. <https://doi.org/10.1128/JB.182.9.2445-2452.2000>.
29. Elias AF, Stewart PE, Grimm D, Caimano MJ, Eggers CH, Tilly K, Bono JL, Akins DR, Radolf JD, Schwan TG, Rosa P. 2002. Clonal polymorphism of *Borrelia burgdorferi* strain B31 Ml: implications for mutagenesis in an infectious strain background. *Infect Immun* 70:2139–2150. <https://doi.org/10.1128/IAI.70.4.2139-2150.2002>.
30. Motaleb MA, Miller MR, Bakker RG, Li C, Charon NW. 2007. Isolation and characterization of chemotaxis mutants of the Lyme disease spirochete *Borrelia burgdorferi* using allelic exchange mutagenesis, flow cytometry, and cell tracking. *Methods Enzymol* 422:421–437. [https://doi.org/10.1016/S0076-6879\(06\)22021-4](https://doi.org/10.1016/S0076-6879(06)22021-4).
31. Sultan SZ, Manne A, Stewart PE, Bestor A, Rosa PA, Charon NW, Motaleb MA. 2013. Motility is crucial for the infectious life cycle of *Borrelia burgdorferi*. *Infect Immun* 81:2012–2021. <https://doi.org/10.1128/IAI.01228-12>.
32. Bertani G. 1951. Studies on lysogenesis. I. The mode of phage liberation by lysogenic *Escherichia coli*. *J Bacteriol* 62:293–300. <https://doi.org/10.1128/jb.62.3.293-300.1951>.
33. Bertani G. 2004. Lysogeny at mid-twentieth century: P1, P2, and other experimental systems. *J Bacteriol* 186:595–600. <https://doi.org/10.1128/JB.186.3.595-600.2004>.
34. Altschul SF, Gish W, Miller W, Myers EW, Lipman DJ. 1990. Basic local alignment search tool. *J Mol Biol* 215:403–410. [https://doi.org/10.1016/S0022-2836\(05\)80360-2](https://doi.org/10.1016/S0022-2836(05)80360-2).
35. Altschul SF, Madden TL, Schäffer AA, Zhang J, Zhang Z, Miller W, Lipman DJ. 1997. Gapped BLAST and PSI-BLAST: a new generation of protein database search programs. *Nucleic Acids Res* 25:3389–3402. <https://doi.org/10.1093/nar/25.17.3389>.
36. Almagro Armenteros JJ, Tsirigos KD, Sønderby CK, Petersen TN, Winther O, Brunak S, von Heijne G, Nielsen H. 2019. SignalP 5.0 improves signal peptide predictions using deep neural networks. *Nat Biotechnol* 37:420–423. <https://doi.org/10.1038/s41587-019-0036-z>.
37. Kall L, Krogh A, Sonnhammer EL. 2005. An HMM posterior decoder for sequence feature prediction that includes homology information. *Bioinformatics* 21(Suppl 1):i251–i257. <https://doi.org/10.1093/bioinformatics/bti1014>.
38. Kall L, Krogh A, Sonnhammer EL. 2007. Advantages of combined transmembrane topology and signal peptide prediction—the Phobius web server. *Nucleic Acids Res* 35:W429–W432. <https://doi.org/10.1093/nar/gkm256>.
39. Marchler-Bauer A, Bo Y, Han L, He J, Lanczycki CJ, Lu S, Chitsaz F, Derbyshire MK, Geer RC, Gonzales NR, Gwadz M, Hurwitz DI, Lu F, Marchler GH, Song JS, Thanki N, Wang Z, Yamashita RA, Zhang D, Zheng C, Geer LY, Bryant SH. 2017. CDD/SPARCLE: functional classification of proteins via subfamily domain architectures. *Nucleic Acids Res* 45:D200–D203. <https://doi.org/10.1093/nar/gkw1129>.
40. Marchler-Bauer A, Derbyshire MK, Gonzales NR, Lu S, Chitsaz F, Geer LY, Geer RC, He J, Gwadz M, Hurwitz DI, Lanczycki CJ, Lu F, Marchler GH, Song JS, Thanki N, Wang Z, Yamashita RA, Zhang D, Zheng C, Bryant SH. 2015. CDD: NCBI's conserved domain database. *Nucleic Acids Res* 43:D222–D226. <https://doi.org/10.1093/nar/gku1221>.
41. El-Gebali S, Mistry J, Bateman A, Eddy SR, Luciani A, Potter SC, Qureshi M, Richardson LJ, Salazar GA, Smart A, Sonnhammer ELL, Hirsh L, Paladin L, Piovesan D, Tosatto SCE, Finn RD. 2019. The Pfam protein families database in 2019. *Nucleic Acids Res* 47:D427–D432. <https://doi.org/10.1093/nar/gky995>.
42. Sonnhammer EL, Eddy SR, Durbin R. 1997. Pfam: a comprehensive database of protein domain families based on seed alignments. *Proteins* 28:405–420. [https://doi.org/10.1002/\(SICI\)1097-0134\(199707\)28:3<405::AID-PROT10>3.0.CO;2-L](https://doi.org/10.1002/(SICI)1097-0134(199707)28:3<405::AID-PROT10>3.0.CO;2-L).
43. Motaleb MA, Corum L, Bono JL, Elias AF, Rosa P, Samuels DS, Charon NW. 2000. *Borrelia burgdorferi* periplasmic flagella have both skeletal and motility functions. *Proc Natl Acad Sci U S A* 97:10899–10904. <https://doi.org/10.1073/pnas.200221797>.
44. Li C, Bakker RG, Motaleb MA, Sartakova ML, Cabello FC, Charon NW. 2002. Asymmetrical flagellar rotation in *Borrelia burgdorferi* nonchemotactic mutants. *Proc Natl Acad Sci U S A* 99:6169–6174. <https://doi.org/10.1073/pnas.092010499>.
45. Barbour AG, Hayes SF, Heiland RA, Schruppf ME, Tessier SL. 1986. A *Borrelia*-specific monoclonal antibody binds to a flagellar epitope. *Infect Immun* 52:549–554. <https://doi.org/10.1128/iai.52.2.549-554.1986>.
46. Carroll JA, El-Hage N, Miller JC, Babb K, Stevenson B. 2001. *Borrelia burgdorferi* RevA antigen is a surface-exposed outer membrane protein whose expression is regulated in response to environmental temperature and pH. *Infect Immun* 69:5286–5293. <https://doi.org/10.1128/IAI.69.9.5286-5293.2001>.
47. Coleman JL, Benach JL. 1992. Characterization of antigenic determinants of *Borrelia burgdorferi* shared by other bacteria. *J Infect Dis* 165:658–666. <https://doi.org/10.1093/infdis/165.4.658>.
48. Toker AS, Macnab RM. 1997. Distinct regions of bacterial flagellar switch protein FLIM interact with FlIG, FlIN and CheY. *J Mol Biol* 273:623–634. <https://doi.org/10.1006/jmbi.1997.1335>.
49. Kariu T, Sharma K, Singh P, Smith AA, Backstedt B, Buyuktanir O, Pal U. 2015. BB0323 and novel virulence determinant BB0238: *Borrelia burgdorferi* proteins that interact with and stabilize each other and are critical for infectivity. *J Infect Dis* 211:462–471. <https://doi.org/10.1093/infdis/jiu460>.
50. Sultan SZ, Pitzer JE, Miller MR, Motaleb MA. 2010. Analysis of a *Borrelia burgdorferi* phosphodiesterase demonstrates a role for cyclic-di-guanosine monophosphate in motility and virulence. *Mol Microbiol* 77:128–142. <https://doi.org/10.1111/j.1365-2958.2010.07191.x>.
51. Novak EA, Sekar P, Xu H, Moon KH, Manne A, Wooten RM, Motaleb MA. 2016. The *Borrelia burgdorferi* CheY3 response regulator is essential for chemotaxis and completion of its natural infection cycle. *Cell Microbiol* 18:1782–1799. <https://doi.org/10.1111/cmi.12617>.
52. Li X, Pal U, Ramamoorthi N, Liu X, Desrosiers DC, Eggers CH, Anderson JF, Radolf JD, Fikrig E. 2007. The Lyme disease agent *Borrelia burgdorferi* requires BB0690, a Dps homologue, to persist within ticks. *Mol Microbiol* 63:694–710. <https://doi.org/10.1111/j.1365-2958.2006.05550.x>.
53. Yang X, Coleman AS, Anguita J, Pal U. 2009. A chromosomally encoded virulence factor protects the Lyme disease pathogen against host-adaptive immunity. *PLoS Pathog* 5:e1000326. <https://doi.org/10.1371/journal.ppat.1000326>.
54. Zhang X, Yang X, Kumar M, Pal U. 2009. BB0323 function is essential for *Borrelia burgdorferi* virulence and persistence through tick-rodent transmission cycle. *J Infect Dis* 200:1318–1330. <https://doi.org/10.1086/605846>.
55. Promnarek K, Kumar M, Shroder DY, Zhang X, Anderson JF, Pal U. 2009. *Borrelia burgdorferi* small lipoprotein Lp6.6 is a member of multiple protein complexes in the outer membrane and facilitates pathogen transmission from ticks to mice. *Mol Microbiol* 74:112–125. <https://doi.org/10.1111/j.1365-2958.2009.06853.x>.
56. Yang X, Lenhart TR, Kariu T, Anguita J, Akins DR, Pal U. 2010. Characterization of unique regions of *Borrelia burgdorferi* surface-located membrane protein 1. *Infect Immun* 78:4477–4487. <https://doi.org/10.1128/IAI.00501-10>.
57. Stewart PE, Bestor A, Cullen JN, Rosa PA. 2008. A tightly regulated surface protein of *Borrelia burgdorferi* is not essential to the mouse-tick infectious cycle. *Infect Immun* 76:1970–1978. <https://doi.org/10.1128/IAI.00714-07>.
58. Hyde JA, Shaw DK, Smith R, III, Trzeciakowski JP, Skare JT. 2009. The BosR regulatory protein of *Borrelia burgdorferi* interfaces with the RpoS regulatory pathway and modulates both the oxidative stress response and pathogenic properties of the Lyme disease spirochete. *Mol Microbiol* 74:1344–1355. <https://doi.org/10.1111/j.1365-2958.2009.06951.x>.
59. Dresser AR, Hardy PO, Chaconas G. 2009. Investigation of the genes involved in antigenic switching at the vlsE locus in *Borrelia burgdorferi*: an essential role for the RuvAB branch migrase. *PLoS Pathog* 5:e1000680. <https://doi.org/10.1371/journal.ppat.1000680>.
60. Pappas CJ, Iyer R, Petzke MM, Caimano MJ, Radolf JD, Schwartz I. 2011. *Borrelia burgdorferi* requires glycerol for maximum fitness during the tick phase of the enzootic cycle. *PLoS Pathog* 7:e1002102. <https://doi.org/10.1371/journal.ppat.1002102>.
61. Miller CL, Karna SL, Seshu J. 2013. *Borrelia* host adaptation regulator (BadR) regulates rpoS to modulate host adaptation and virulence factors in *Borrelia burgdorferi*. *Mol Microbiol* 88:105–124. <https://doi.org/10.1111/mmi.12171>.
62. Kung F, Kaur S, Smith AA, Yang X, Wilder CN, Sharma K, Buyuktanir O, Pal U. 2016. A *Borrelia burgdorferi* surface-exposed transmembrane protein lacking detectable immune responses supports pathogen persistence and constitutes a vaccine target. *J Infect Dis* 213:1786–1795. <https://doi.org/10.1093/infdis/jiw013>.

63. Xu H, Sultan S, Yerge A, Moon KH, Wooten RM, Motaleb MA. 2017. *Borrelia burgdorferi* CheY2 is dispensable for chemotaxis or motility but crucial for the infectious life cycle of the spirochete. *Infect Immun* 85:e00264. <https://doi.org/10.1128/IAI.00264-16>.
64. Ramsey ME, Hyde JA, Medina-Perez DN, Lin T, Gao L, Lundt ME, Li X, Norris SJ, Skare JT, Hu LT. 2017. A high-throughput genetic screen identifies previously uncharacterized *Borrelia burgdorferi* genes important for resistance against reactive oxygen and nitrogen species. *PLoS Pathog* 13:e1006225. <https://doi.org/10.1371/journal.ppat.1006225>.
65. Motaleb MA, Sultan SZ, Miller MR, Li C, Charon NW. 2011. CheY3 of *Borrelia burgdorferi* is the key response regulator essential for chemotaxis and forms a long-lived phosphorylated intermediate. *J Bacteriol* 193:3332–3341. <https://doi.org/10.1128/JB.00362-11>.
66. Mastronarde DN. 2005. Automated electron microscope tomography using robust prediction of specimen movements. *J Struct Biol* 152:36–51. <https://doi.org/10.1016/j.jsb.2005.07.007>.
67. Zheng SQ, Palovcak E, Armache J-P, Verba KA, Cheng Y, Agard DA. 2017. MotionCor2: anisotropic correction of beam-induced motion for improved cryo-electron microscopy. *Nat Methods* 14:331–332. <https://doi.org/10.1038/nmeth.4193>.
68. Kremer JR, Mastronarde DN, McIntosh JR. 1996. Computer visualization of three-dimensional image data using IMOD. *J Struct Biol* 116:71–76. <https://doi.org/10.1006/jsbi.1996.0013>.
69. Agulleiro J-I, Fernandez J-J. 2015. Tomo3D 2.0 – exploitation of advanced vector eXtensions (AVX) for 3D reconstruction. *J Struct Biol* 189:147–152. <https://doi.org/10.1016/j.jsb.2014.11.009>.
70. Zhang K. 2016. Gctf: real-time CTF determination and correction. *J Struct Biol* 193:1–12. <https://doi.org/10.1016/j.jsb.2015.11.003>.
71. Winkler H. 2007. 3D reconstruction and processing of volumetric data in cryo-electron tomography. *J Struct Biol* 157:126–137. <https://doi.org/10.1016/j.jsb.2006.07.014>.
72. Winkler H, Zhu P, Liu J, Ye F, Roux KH, Taylor KA. 2009. Tomographic sub-volume alignment and subvolume classification applied to myosin V and SIV envelope spikes. *J Struct Biol* 165:64–77. <https://doi.org/10.1016/j.jsb.2008.10.004>.
73. Pettersen EF, Goddard TD, Huang CC, Couch GS, Greenblatt DM, Meng EC, Ferrin TE. 2004. UCSF Chimera—a visualization system for exploratory research and analysis. *J Comput Chem* 25:1605–1612. <https://doi.org/10.1002/jcc.20084>.
74. Goddard TD, Huang CC, Meng EC, Pettersen EF, Couch GS, Morris JH, Ferrin TE. 2018. UCSF ChimeraX: meeting modern challenges in visualization and analysis. *Protein Sci* 27:14–25. <https://doi.org/10.1002/pro.3235>.